Journal of Power Sources 233 (2013) 346–357

Contents lists available at SciVerse ScienceDirect

Journal of Power Sources

journal homepage: www.elsevier.com/locate/jpowsour

Improving high-capacity $Li_{1.2}Ni_{0.15}Mn_{0.55}Co_{0.1}O_2$-based lithium-ion cells by modifiying the positive electrode with alumina

Martin Bettge [a], Yan Li [a,b], Bharat Sankaran [c], Nancy Dietz Rago [a], Timothy Spila [c], Richard T. Haasch [c], Ivan Petrov [c], Daniel P. Abraham [a,*]

[a] Chemical Sciences and Engineering Div., Argonne National Laboratory, 9700 S. Cass Ave. Lemont, Argonne, IL 60439, USA
[b] Materials Science Program, University of Rochester, RC Box 270216, Rochester, NY 14627-0216, USA
[c] Frederick-Seitz Materials Research Laboratory, University of Illinois at Urbana-Champaign, 104 S. Goodwin Ave., Urbana, IL 61801, USA

HIGHLIGHTS

- ► Positive electrodes in Li-ion full-cells are modified by thin Al_2O_3 coatings and alumina powder.
- ► ALD-Al_2O_3 coatings (<4 nm) improve very effectively capacity retention and transport kinetics.
- ► The coatings are partially dissolved and affect surface films on the negative electrode.
- ► The coatings only delay, but do not prevent, full-cell degradation during extended cycling.

GRAPHICAL ABSTRACT

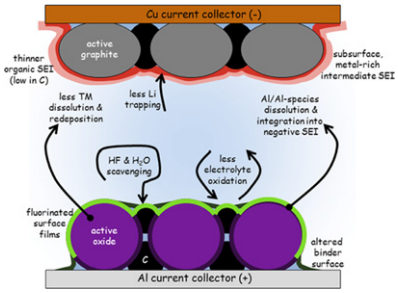

ARTICLE INFO

Article history:
Received 7 December 2012
Received in revised form
13 January 2013
Accepted 16 January 2013
Available online 29 January 2013

Keywords:
Lithium-ion
Atomic layer deposition
Al_2O_3
Coating
Secondary ion mass spectrometry
Layered oxide

ABSTRACT

Practical high-capacity Li-ion cells containing $Li_{1.2}Ni_{0.15}Mn_{0.55}Co_{0.1}O_2$-based positive and graphite-based negative electrodes show substantial capacity loss and impedance rise when repeatedly cycled to, or held for extended periods, at voltages exceeding 4.5 V. Their performance can be effectively improved by modifying the positive electrode. The positive composite electrodes are modified here in two different ways: by (i) alumina coatings of up to ~4 nm applied via atomic layer deposition (ALD), and (ii) addition of nanoscale alumina powder. Thicknesses of the ALD coatings are estimated via X-ray photoelectron spectroscopy (XPS).

Electrochemical cycling reveals that capacity retention is better, and impedance rise is smaller for cells containing ALD-coated electrodes. Cells with alumina-powder modified electrodes show also improved capacity retention, but without improvements in impedance. Improved capacity retention is primarily due to reduced Li trapping on the negative electrode. Lower impedance growth, in ALD modified cells, is attributed to improved electro-mechanical integrity and altered surface films inside the positive electrode. The alumina coating inhibits, but does not prevent, transition metal dissolution. The coating also reduces electrolyte oxidation. Significant accumulation of Al on the negative electrode indicates electrochemical crosstalk between the electrodes and chemical instability of the ALD coatings during extended cycling.

© 2013 Elsevier B.V. All rights reserved.

* Corresponding author.
E-mail addresses: bettge@anl.gov (M. Bettge), liy@anl.gov (Y. Li), bharat.sankaran@gmail.com (B. Sankaran), dietz@anl.gov (N.D. Rago), tspila@illinois.edu (T. Spila), r-haasch@illinois.edu (R.T. Haasch), petrov@illinois.edu (I. Petrov), abraham@anl.gov (D.P. Abraham).

0378-7753/$ – see front matter © 2013 Elsevier B.V. All rights reserved.
http://dx.doi.org/10.1016/j.jpowsour.2013.01.082

1. Introduction

For lithium-ion batteries to widely power plug-in hybrid electric and all-electric vehicles (PHEVs and EVs), they must meet a range of stringent criteria: for instance, energy densities high enough to allow for more than 100 miles of travel autonomy at low costs (in terms of $-Wh^{-1} or $-kg^{-1}); as well as moderate, but consistent, power densities throughout the entire state-of-charge (SOC) range. Other requirements include good safety, a 10 year calendar-life and a cycle-life of up to a few thousand charge and discharge cycles [1–3]. Batteries containing lithium- and manganese-rich layered-oxides (LMR-NMC) as positive electrode materials can meet some of these requirements [4–6]. Theoretical charge and energy densities exceeding 250 Ah-kg^{-1} and 900 Wh-kg^{-1} can be achieved when these materials are charged beyond 4.5 V vs. Li^+/Li. However, battery life requirements remain a serious challenge for this class of materials when repeatedly cycled, or when held at high voltages for extended periods.

At high operating cell potentials (>4.0 V vs. Li^+/Li), the electrolyte and its constituents are exposed to strongly reducing and oxidizing conditions on anode and cathode surfaces, respectively. The reduction reactions on the negative side have been extensively studied and found to be largely suppressed by the formation of a stable solid–electrolyte-interface (SEI) [7,8]. The oxidation reactions on the positive side, which are much less understood, are known to trigger rising cell resistances and continuous capacity losses, in $LiNi_{0.8}Co_{0.2-x}Al_xO_2$ and the high-capacity LMR-NMC materials [5,9–15].

One particularly effective strategy to improve cell performance is to apply single-particle and/or conformal coatings to the positive electrode [16–18]. Depending on the materials applied, it is believed that coatings can generally i) enhance the electronic conductivity within the electrode laminate, ii) improve the surface stability of the coated materials, or iii) simply provide a physical barrier that suppresses any detrimental chemical side reactions between electrode surface and electrolyte. Certain oxide coatings may also lower the acidity of the non-aqueous electrolytes by scavenging hydrogen fluoride (HF) and thus reducing metal dissolution from the active materials in the electrode [19–21].

Here, we apply a thin coating of alumina via atomic layer deposition (ALD) onto composite electrodes to improve cycle- and calendar-life of full-cells in which an LMR-NMC material is galvanostatically cycled versus graphite. Several reasons prompt this effort: First of all, previous studies have demonstrated improved half-cell performance of alumina-coated composite electrodes containing lithium cobalt oxide and lithium-excess layered oxides [17,22–25] justifying the expectation of an improved performance in practical full-cells. There is also an inherent advantage of conformally coating the entire laminate *after* casting, drying, and rolling over coating single particles prior: insulating particle coatings increase electronic contact resistance, while laminate coatings leave the particle–particle interfaces unaltered [17,22] and may even protect the surfaces of the other electrode constituents. ALD is the technique of choice: it is well-established and provides a uniform and conformal Angstrom-scale coating through self-limiting surface reactions [26]. Such level of control is imperative, as the electrochemical surface area of the porous composite electrodes is very high and can readily exceed 100 m^2 per m^2 of the electrode depending on particle morphologies and electrode loading density. The material of choice is alumina: it can be readily deposited by ALD [26] and it is electronically a wide band-gap material, yet penetrable to ions [27]. Diffusion of lithium is thus possible while electronic transport across the solid–electrolyte interfaces is curbed slowing parasitic oxidation reactions.

We also find that the mere addition of alumina powder to the positive electrode coating can improve cell capacity retention, showing the importance of HF- and water-scavenging. The discussion of how these two alumina-based electrode modifications impact practical full-cell performance is at the heart of this paper.

2. Experimental

2.1. Materials

Table 1 details electrode formulation and chemistry of our electrochemical cells. The active LMR-NMC material of the positive electrode is $Li_{1.2}Ni_{0.15}Mn_{0.55}Co_{0.1}O_2$, expressed as $0.5Li_2MnO_3 \cdot 0.5LiMn_{0.375}Ni_{0.375}Co_{0.25}O_2$ in the two-component notation, with a theoretical capacity of 377 mAh-g^{-1} upon full removal of lithium. SuperP and graphite form the current carrying network through the laminate held together by a PVdF binder. The active material of the negative electrode is graphite; the electrode also contains SuperP for improved electronic conductivity and a PVdF binder. All cells contain a $LiPF_6$-based electrolyte (also known as "Gen2") and a polypropylene–polyethylene–polypropylene trilayer separator.

Positive electrodes are modified by alumina in two different ways: (i) coating of the positive laminate (Table 1) with alumina via ALD, and (ii) blending 5 wt.% Al_2O_3 nanosized powder with the other electrode constituents of the positive laminate (Table 1). The Al_2O_3 powder has a particle size of ~50 nm and a high surface area (32–40 m^2-g). To ensure adequate dispersion, the Al_2O_3 powder is mixed into the NMP (*N*-Methyl-2-pyrrolidone, NMP) at the very beginning of the slurry making process.

The ALD coatings are applied to the electrode laminates (not to individual particles) in a Cambridge Nanotech Savannah 100 deposition tool at a relatively low temperature (80 °C) to minimize PVdF binder degradation. ALD uses sequential pulsing of precursor vapors, each of which forms approximately one atomic layer of material per pulse. During the initial cycle, the first precursor, H_2O, is pulsed into the chamber and exposed to the electrode for 1 s. The

Table 1
Electrode chemistry and formulation.

	As-prepared and ALD-modified positive electrodes	Powder-modified positive electrode	Negative electrode
Active material	86 wt.% $Li_{1.2}Ni_{0.15}Mn_{0.55}Co_{0.1}O_2$ (Toda HE5050)	80 wt.% $Li_{1.2}Ni_{0.15}Mn_{0.55}Co_{0.1}O_2$ (Toda HE5050)	90 wt.% A12 graphite (ConocoPhillips)
Binder	8 wt.% PVdF (Solvay 5130)	8 wt.% PVdF (Solvay 5130)	6 wt.% PVdF (Kureha, KF-9300)
Additives	4 wt.% SFG-6 graphite (Timcal)	2 wt.% SFG-6 graphite (Timcal)	
	2 wt.% SuperP (Timcal)	5 wt.% SuperP (Timcal)	4 wt.% SuperP (Timcal)
		5 wt.% Al_2O_3 (AlfaAesar)	
Current collector	Al, 15 μm	Al, 20 μm	Cu, 10 μm
Active loading density	6.64 mg-cm^{-2}	3.5 mg-cm^{-2}	5.61 mg-cm^{-2}
Electrode porosity	37%	44%	26%
Laminate thickness	35 μm	22 μm	40 μm
Electrolyte	1.2 M $LiPF_6$ in ethylene carbonate:ethyl methyl carbonate (3:7 by wt.)		
Separator	25 μm thick (Celgard 2325)		

reaction chamber is then evacuated for 65 s to remove any residual gaseous species. Subsequently, the second precursor, trimethylaluminum (TMA), is pulsed into the chamber; again, exposure time is 1 s. The reaction chamber is then evacuated again for 65 s to remove the gaseous by-products and excess TMA. This ends the first cycle and the procedure is repeated until the target alumina thickness is achieved. From the second cycle on, the overall reaction is $3H_2O + 2Al(CH_3)_3 \rightarrow Al_2O_3 + 6CH_4$. Further details on the associated surface reactions are described elsewhere [26–28].

2.2. Electrochemical characterization

Electrochemical cycling experiments are conducted in 2032-type coin cells (1.6 cm^2 area electrodes). Our coin cells are assembled in an Ar-atmosphere glove box ($O_2 < 10$ ppm, $H_2O < 1$ ppm) and galvanostatically cycled within a constant temperature oven held at 30 °C. Formation cycling of full-cells is carried out in two steps. The cells are first cycled three times between 2.2 and 4.1 V to enable complete wetting of the electrochemically active surfaces, followed by two cycles between 2.2 and 4.6 V to "activate" the oxide material; a 0.16 mA (15 mA g^{-1}-oxide) current is used in both steps. Extended cycling is conducted for 50 cycles between 2.2 and 4.6 V with a 0.8 mA (75 mA g^{-1}-oxide) current; this is followed by two lower current (0.16 mA) cycles to determine the true loss of lithium during cycling/aging by minimizing impedance effects in the capacity–voltage profiles.

AC impedance spectroscopy is carried out after the initial formation cycles and after extended cycling. An EG&G 273A potentiostat and a Solartron SI1260 frequency response analyzer controlled by ZPLOT measurement software are used. The cells are charged to 3.75 V and held at the voltage for ~15 h before collecting the impedance data at 30 °C in the 100 kHz–10 mHz frequency range, with a 10 mV perturbation around the open-circuit voltage. The 3.75 V value was chosen because the cells' internal resistance is close to a minimum at this voltage [29].

2.3. Microscopy and spectroscopy

Imaging using scanning electron microscopy (SEM) and elemental analysis using energy dispersive X-ray spectroscopy (EDS) are carried out on a field emission scanning electron microscope (JEOL JSM7500F) equipped with a Thermo Fisher energy dispersive X-ray analysis unit. Information on elemental distribution and particle morphology is obtained from the data.

Elemental surface analysis on the positive electrodes via X-ray photoelectron spectroscopy (XPS) is carried out on a Kratos Axis Ultra X-ray photoelectron spectrometer under ultrahigh vacuum (10^{-9} Torr) conditions, and with monochromatic Al K_α ~1486.6 eV radiation as the primary excitation source. In XPS, an incident beam of monoenergetic X-rays produces photoelectron emission from the sample surface. The binding energy of the ejected photoelectron provides elemental composition and chemical state information. XPS on the positive electrode probes a depth of ~2–5 nm with a lateral resolution of ~1 mm. Peak fits of all spectra are performed using the Shirley background correction and Gaussian–Lorentzian curve synthesis. The energy scale is adjusted based on the graphite peak in the C1s spectrum at 284.5 eV.

Dynamic SIMS experiments on the negative electrodes are conducted on a Cameca IMS-5F system using a 12 kV O^{2+} primary ions with a beam current of 20 nA. Positive secondary ions are detected. Elemental depth profiles are obtained with a raster size of 250 × 250 μm and an image field of 150 μm, and each species is analyzed for 1 s before switching to the next one. In SIMS, samples bombarded with energetic (tens of keV) primary ions eject secondary atoms and ions from the top layer of surface molecules; the ejected ions are subsequently accelerated into a mass spectrometer, where they are separated and counted based on their mass-to-charge ratio. SIMS is a powerful technique for probing cycled negative electrodes because of its excellent detection limits (ppb to ppm) and good depth resolution [30].

3. Results

3.1. Electrochemical examination

Fig. 1A and B contains the initial voltage profiles and the electrochemical cycling plots, respectively, from baseline full-cells containing the as-prepared positive electrodes. The charge and discharge capacities for the first 2.2–4.1 V cycle are 89 mAh-g^{-1} and 64 mAh-g^{-1} respectively (Fig. 1A), which are significantly lower than typical values for $LiNi_{0.8}Co_{0.15}Al_{0.05}O_2$-bearing cells (~160 mAh-g^{-1}) cycled in the same voltage window [31]. Electrochemical activation of the oxide particles, seen as a ~4.4 V plateau in the first 2.2–4.6 V cycle, is needed to achieve the high discharge capacity (>250 mAh-g^{-1}). This activation is typically associated with structural changes and loss of oxygen from the oxide [5,32,33]. During extended cycling over 50 cycles, the full-cells typically show coulombic efficiencies of ~99.5%. The baseline cell in Fig. 1B steadily losses capacity at a rate of 0.48% per cycle. Full-cells containing the alumina-coated and powder-modified positive electrodes show similar voltage profiles during the first cycles demonstrating that

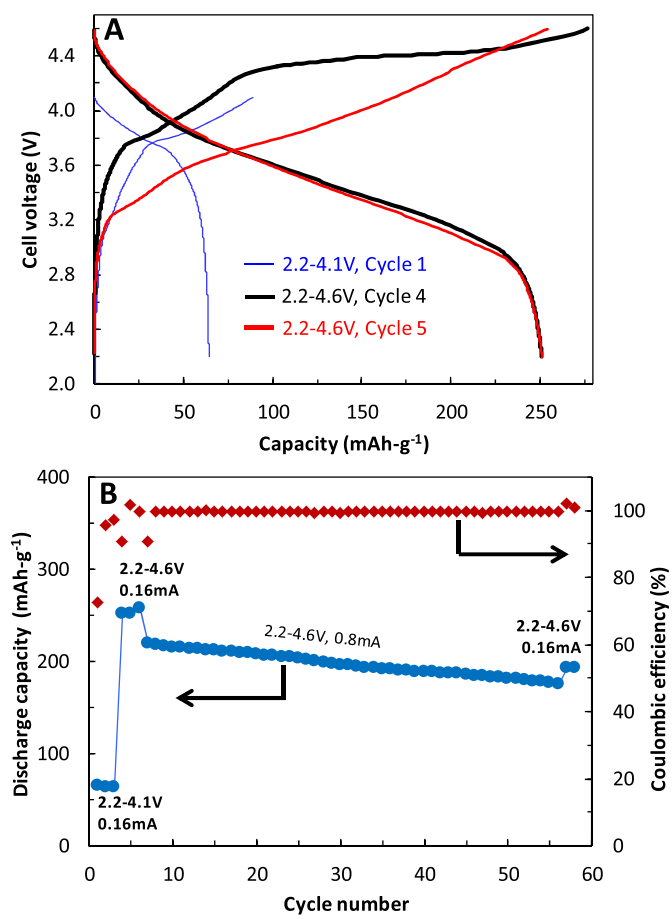

Fig. 1. Cycle plots for full-cells containing the as-prepared (0 nm) electrode showing in A) the first 2.2–4.1 V cycle, and the first and second 2.2–4.6 V cycles, and in B) discharge capacity and columbic efficiency changes with cycle number. Voltage ranges and cycling currents are as indicated; capacities are based on the oxide particle content in the positive electrodes.

the alumina presence does not alter the initial charge–discharge cycling characteristics in any significant manner.

However, the rate at which capacity fades is lower for samples with an alumina coating. Fig. 2 details voltage profiles and capacity retention at relatively low (Fig. 2A) and moderate (Fig. 2B) cycling rates; normalized capacity data are shown to account for normal cell to cell variations that result from small differences in electrode loading, coin cell construction, etc. A distinct trend is seen after fifty 2.2–4.6 V cycles; capacity retention clearly improves with increasing thickness of the alumina coating.

Fig. 3 contains AC impedance spectra from full-cells showing the effect of coating the positive electrodes with ALD alumina; the spectra include contributions from all cell components after the initial cycles (Fig. 3A) and 50 cycles (Fig. 3B). A typical complex impedance plot for as-prepared baseline cells shows several features: (i) a high frequency minimum (at 100 kHz) that relates to the ohmic portion of the electrode impedance and includes contributions from the electronic conductivity of the electrodes and ionic conductivity of the electrolyte solution, as well as any electronic contact resistances associated with the cell hardware, current collectors, and electrode materials; (ii) two major arcs with their maxima located in the 10 kHz to ~1 Hz range. These frequencies are generally associated with charge transport across the particle–particle and particle–electrolyte interfaces; (iii) a Warburg impedance tail at frequencies <1 Hz, which is associated with bulk diffusional effects in the cell, including diffusion of salt in the electrolyte and of lithium within the electrode active materials [11–13,34].

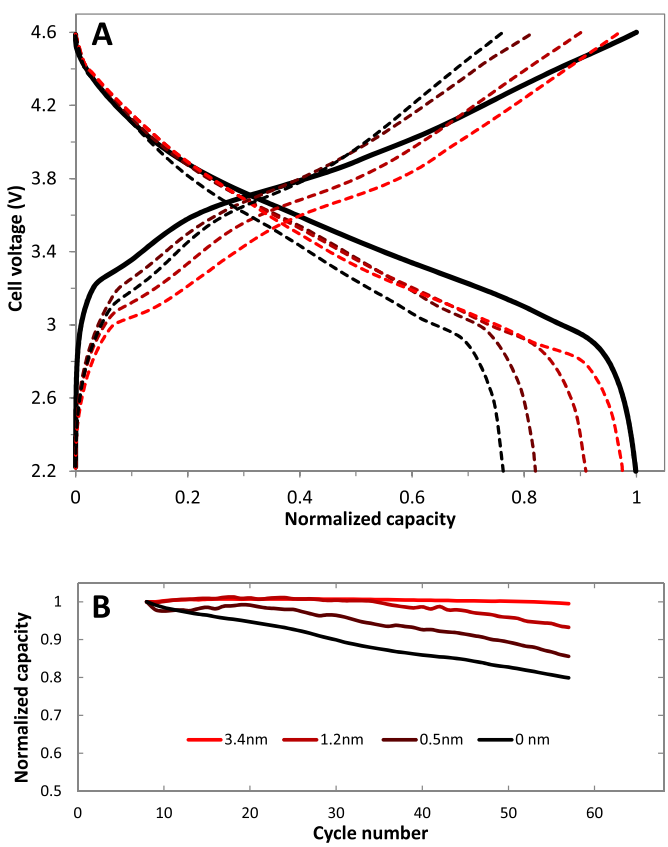

Fig. 2. Improving capacity retention by ALD coating positive electrodes with Al_2O_3: A) voltage profiles at ~C/16 rate before and after 50 cycles. The normalized capacity value of 1 is ~250 mAh-g^{-1} with respect to the oxide particle loading. The initial charge–discharge cycles for all cells are very similar, and hence only one typical plot is shown. B) Normalized capacity vs. cycle number at a moderate current (~C/3 rate) in the 2.2–4.6 V cycling window. At this rate, a normalized capacity value of 1 equals ~220 mAh-g^{-1}.

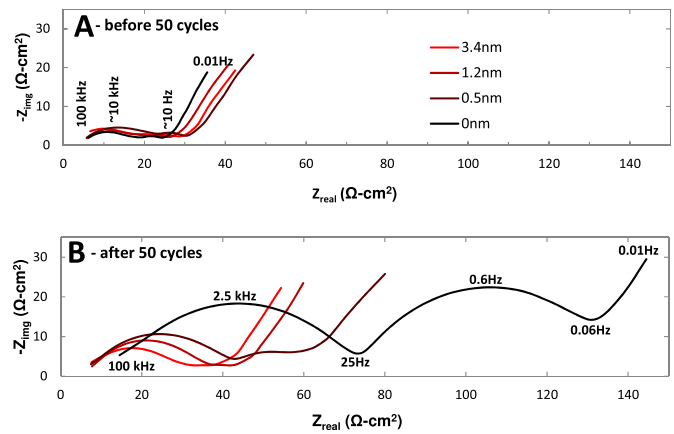

Fig. 3. Improving full-cell AC impedance by ALD coating positive electrodes with alumina. Electrochemical impedance spectra (100 kHz–0.01 Hz, at 30 °C and 3.75 V) showing the effect of 0, 0.5 nm, 1.2 nm and 3.4 nm thick alumina coatings on impedance after A) initial cycles and after B) fifty 2.2–4.6 V cycles. Frequency values, for the 0 nm cell, are shown in both A and B.

All cells show similar impedances after the initial cycles (Fig. 3A). But major differences are observed after fifty 2.2–4.6 V cycles (Fig. 3B): cells containing the as-prepared (0 nm coating thickness) electrode show much greater rise in impedances than cells containing the coated positive electrodes. In fact, the impedances decrease with increasing coating thickness. All cells are affected by impedance rise over the entire frequency range, as shown in Fig. 3A and B. This impedance rise occurs primarily at the positive electrode, as separate three-electrode measurements have confirmed [15,35]. The spectrum of the baseline cell is dominated by two arcs with maxima shifted down to 2.5 kHz (from 10 kHz) and 0.6 Hz (from 10 Hz) after cycling. The high-frequency arc, at 2.5 kHz, arises primarily from a degradation of the electronic network that links the oxide particles to the current collector; the mid-frequency arc, at 0.6 Hz, can be mostly attributed to processes at the oxide–electrolyte interfaces that impede the motion of lithium ions. Both arcs decrease with increasing coating thickness, resulting in overall lower impedances for the ALD-modified cells after 50 cycles. In fact, the mid-frequency arc nearly disappears for the cell containing the 3.4 nm coated positive electrode. These results suggest that the alumina coating stabilizes the electronic network, as well as the oxide–electrolyte interfaces.

Fig. 4 shows cycling data and impedance spectra from full-cells containing the alumina-powder modified positive electrode. These electrodes complement our ALD experiments: the total surface area of the alumina powder added (5 wt.%) is on the order of the total electrode's surface area, and thus comparable to the ALD-modified electrodes. The impedance rise of these cells is similar to that of the as-prepared (0 nm) electrodes, i.e., addition of the alumina powder does not alter the positive electrode and its impedance. Capacity retention, on the other hand, is much improved: at a ~C/3 rate, a capacity fade of ~0.12% per cycle is measured versus 0.48% per cycle for the baseline cell. This also confirms that capacity fade is largely independent from cell impedance rise.

3.2. SEM, EDS and XPS on positive electrodes before cycling

Typical micrographs of our positive electrode laminate, as in the top-left of Fig. 5, show ~5 μm sized oxide particles that are composed of much smaller randomly oriented plate-like particles. The ~5 μm sized graphite particles appear darker. The alumina coating cannot be identified in SEM images, but is evident in X-ray

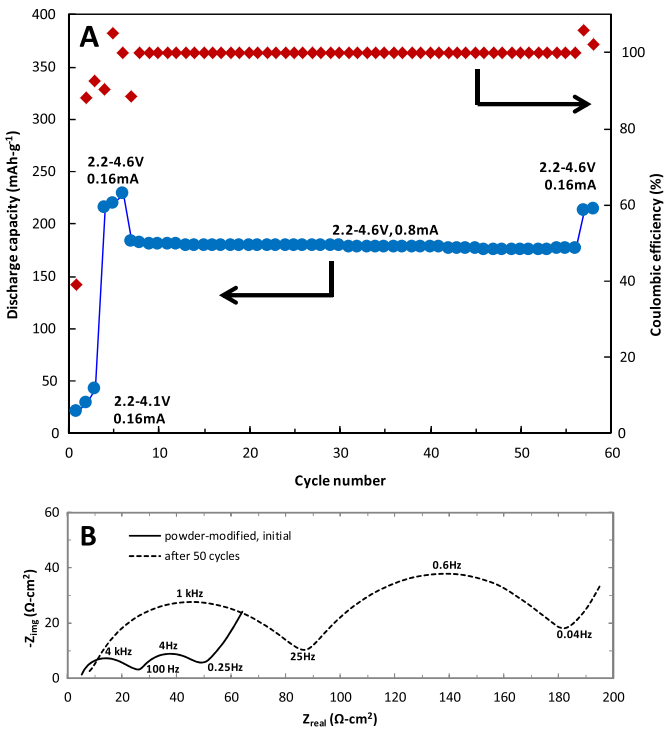

Fig. 4. Plots for full-cells containing the alumina-powder modified positive electrode showing A) changes in discharge capacity and columbic efficiency with cycle number; voltage windows are given and cycling currents are based on oxide particle content in the positive electrode; B) impedance spectra (100 kHz–0.01 Hz, at 30 °C and 3.75 V) after initial cycles and after fifty 2.2–4.6 V cycles.

elemental maps generated by EDS. In Fig. 5, the C map, primarily from graphite and SuperP, and the F map, primarily from the PVdF binder, are compared to the Al map. It is evident that Al is uniformly distributed over the positive electrode surface, indicating that all electrode constituents, including the binder, are covered by the coating. No Al is detected on uncoated electrodes.

XPS is used to estimate the thickness of the ALD alumina layer covering the top surface of the positive electrodes in the following manner. First, alumina is deposited onto a Si(100) substrate that is placed alongside a positive electrode during coating. Assuming a thin alumina layer, of thickness t, on top of a semi-infinite Si substrate, t can be calculated from the ratio of the I_{Al2p} and I_{Si2p} peak intensities [36]; these intensities are proportional to the area under the Al2p and Si2p XPS peaks. Intensity attenuation by inelastic electron scattering is a function of depth, d, and take-off angle, θ, and is defined by the Beer–Lambert relationship, $I = I_0\exp(-d/\lambda\sin\theta)$. With this equation, a ratio of the intensity of the overlayer, alumina, and the substrate, silica, can be defined. Integration and rearrangement of the ratio of intensities yields the following:

$$t_{Al_2O_3} = -\ln\left[\frac{nSi\cdot\rho Al_2O_3\cdot\lambda Al_2O_3}{nAl_2O_3\cdot\rho Si\cdot\lambda Si + nSi\cdot\rho Al_2O_3\cdot\lambda Al_2O_3}\right]\cdot\lambda_{Al_2O_3}\cdot\sin\theta \quad (1)$$

Here, $t_{Al_2O_3}$ = thickness of Al_2O_3 on the planar Si substrate, $\lambda_{Al_2O_3}$ = inelastic mean-free path (IMFP) for an electron with the kinetic energy of an Al2p electron traveling through Al_2O_3 (3.28 nm) [37], λ_{Si} = IMFP for an electron with the kinetic energy of an Si2p electron traveling through Al_2O_3 (3.233 nm) [37], $\rho_{Al_2O_3}$ = mole density of alumina (0.0777 cm^{-3}), ρ_{Si} = mole density of Si (0.0826 cm^{-3}), and $\theta = 90°$; values n_{Si} = number of Si atoms, and $n_{Al_2O_3}$ = number of Al_2O_3 units, are obtained from the Al2p and Si2p atomic concentrations, respectively, calculated from the fitted XPS data.

Second, the (Al + O)/C surface concentration ratio, R, is measured from the Al2p, O1s, and C1s peaks for each alumina-coated positive electrode. The $t_{Al_2O_3}$ can then be plotted and expressed as a function of R making thickness calibration for composite electrodes possible. In Fig. 6, $t_{Al_2O_3}$ and R are both plotted against the

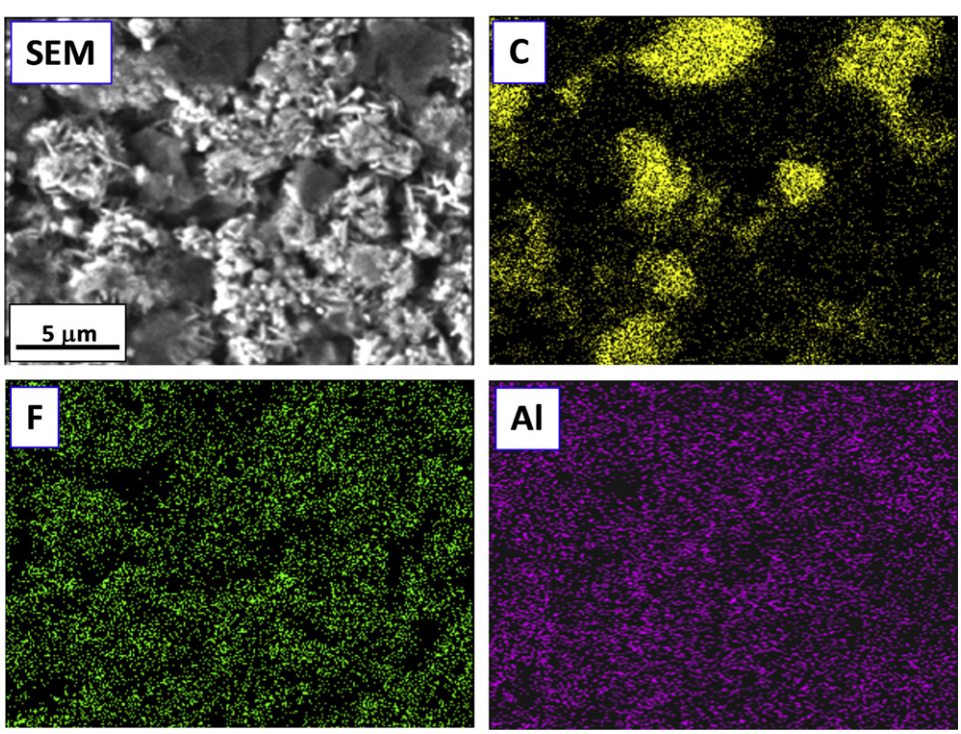

Fig. 5. SEM image of top electrode surface with C, F and Al elemental maps from EDS analysis after 3.4 nm thick ALD alumina coating. The elemental signals are from conductive carbon additives, PVdF binder, and alumina, respectively.

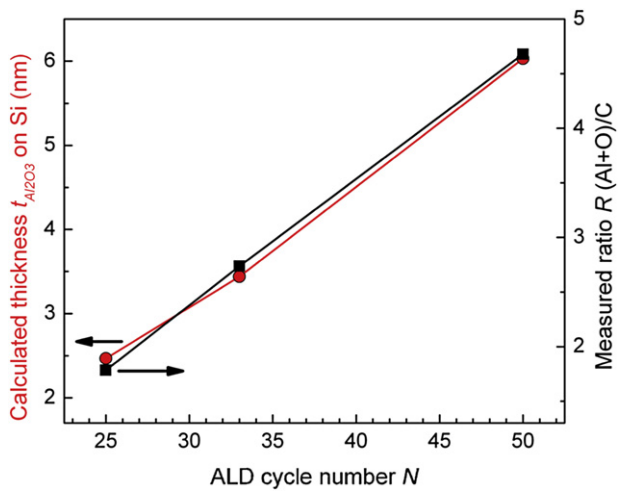

Fig. 6. Al_2O_3 thickness on planar Si(100) and (Al + O)/C concentration ratio from the positive electrode plotted against the number of ALD cycles; this plot makes thickness estimation by XPS possible.

number of ALD cycles to highlight the consistency of our approach. The $t_{Al_2O_3}$ vs. R calibration used herein is $t_{Al_2O_3} = 1.25R + 0.16$. Note that $t_{Al_2O_3}$ is an "equivalent thickness" on a planar Si substrate: we use this thickness throughout this article to denote the alumina coating thickness on our positive electrodes.

Fig. 7 provides XPS spectra from as-prepared and alumina-coated positive electrodes. Table 2 lists concentrations of the four predominant elements, C, O, F, and Al. The coating thicknesses are based on the $t_{Al_2O_3}$ vs. R calibration equation. For the as-prepared samples, the C1s spectrum contains contributions from graphite (284.5 eV), SuperP carbons (285 eV), and the PVdF [−(CH2CF2)$_x$] binder (286.4 eV, 290.9 eV). The F1s spectrum shows a strong peak at 687.8 eV from the PVdF binder. The O1s spectrum shows a peak at 529.6 eV from the $Li_{1.2}Ni_{0.15}Mn_{0.55}Co_{0.1}O_2$, and a weak, broad peak centered at 532 eV that may be from a Li_2CO_3 impurity that is known to form on these oxides [8].

Table 2
Surface concentrations[a] calculated from XPS spectra for as-prepared and alumina-coated electrodes.

Electrodes labeled according to estimated Al_2O_3 thicknesses	C1s(%)	O1s(%)	F1s(%)	Al2p(%)
As-prepared (0 nm)	65.5	10.1	24.5	0
0.5 nm	58.7	14.6	24.1	2.7
1.2 nm	44.9	26.2	17.3	11.6
3.4 nm	25.1	49.4	9.0	16.5

[a] Surface concentrations measured relative to the total (C1s + O1s + F1s + Al2p) intensity.

For the coated cathodes, the O1s and Al2p spectra show that concentration of Al and O increases with increasing alumina thickness (also see Table 2). In contrast, reductions are observed in peak intensities that arise from graphite/SuperP, PVdF and the LMR-NMC particles, which indicate that all electrode components are covered by the alumina coating. After coating, peak shifts associated with the PVdF binder are observed in both the F1s and C1s spectra: these shifts may result from Al-doping of the polymeric binder [38]. A new broad peak centered at 685.5 eV also appears in the F1s spectrum, indicating the presence of other fluorinated compounds, such as AlO_xF_y [39]. The presence of remnant graphite, binder, and oxide peaks in the C1s, F1s and O1s spectra indicates

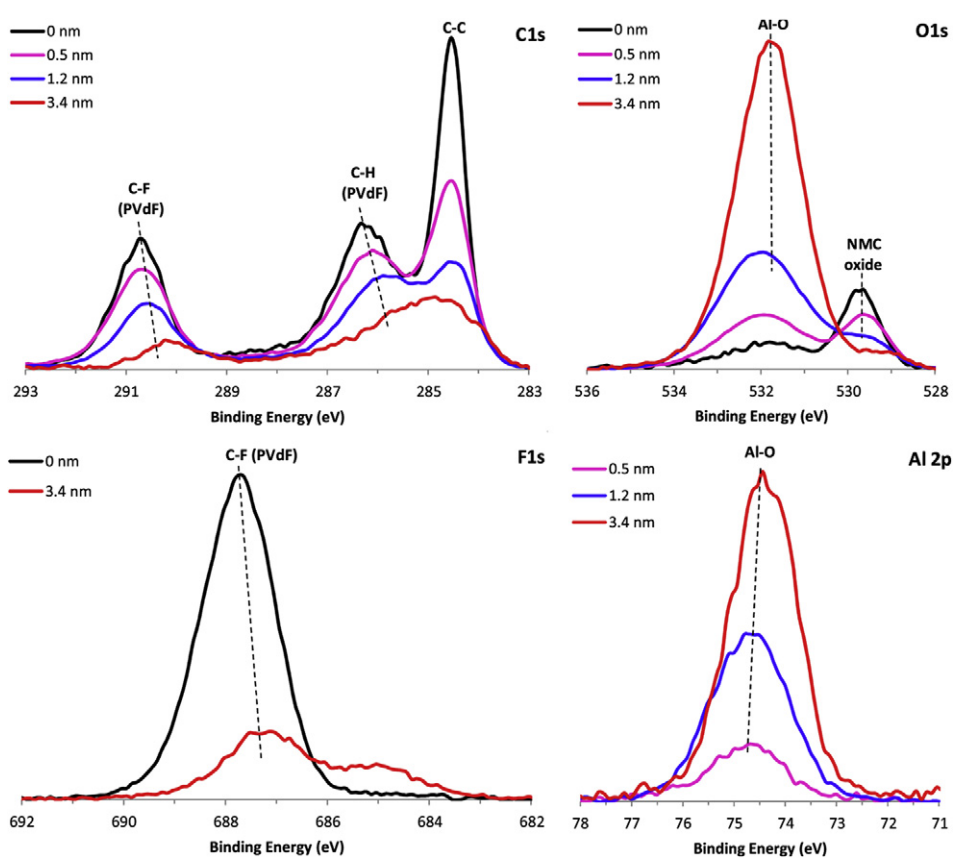

Fig. 7. XPS spectra showing the changes induced on positive electrode surfaces by alumina immediately after the ALD process.

that the alumina coatings are on average less than ~5 nm thick, thin enough for photoelectrons to escape from the underlying layers.

3.3. XPS on ALD-coated positive electrodes after cycling

Figs. 8 and 9 display the changes induced by electrochemical cycling for the as-prepared (0 nm) and alumina-coated (3.4 nm) positive electrodes, respectively.

In Fig. 8, the C1s spectrum from the as-prepared (0 nm) sample shows a reduction in the graphite, SuperP, and PVdF peak intensities on electrochemical cycling. Reduction in the binder (C–F) peak intensity is also seen in the F1s spectrum, which also shows a peak that likely arises from LiF. The O1s spectrum shows the most significant changes that include an intensity reduction of the oxide peak, which is consistent with the observed reduction in the Mn3p, Co3p, and Ni3p peak intensities. According to peak fits (not shown), additional peaks with intensities centered at 532.4 eV (C=O) and 534.2 eV are also observed. The C1s intensity at 286.8 eV (C*O(O)C=O), along with intensities at 532.4 eV (CO(O)C=O*) and 533.5 eV (CO*(O)C=O) suggest the presence of alkyl carbonates. The 534.2 eV also includes contributions from P–O functional groups that are also seen in the P2p spectrum (~135 eV, not shown here). The XPS data indicate that the cycled electrodes have distinct surface films containing compounds that include LiF, $Li_xPO_yF_z$, and alkyl carbonates, consistent with observations on other lithium-based metal-oxide compounds [8].

In Fig. 9, the C1s spectrum shows higher intensities for the cycled samples with peaks centered at 284.7 eV (C–C), 286.7 eV (C–O) and 288.7 eV. Note that the 288.7 peak, which is absent in the 0 nm cycled sample, may indicate the presence of oxidized carbons (O–C=O), or hydroxylated carbons (C–OH). The Al2p peak of the alumina-coated sample shows a very distinct reduction in intensity on cycling, along with a reduction in Al–O peak intensity in the O1s spectrum. A lack of intensity at 529.5 eV, indicates complete coverage of the oxide particles by overlying films following electrochemical cycling. A new peak around 533 eV also appears, is possibly related to (C=O)-bonding. The F1s spectrum shows a reduction in PVdF and 685 eV peak intensities, but a new peak centered on ~686 eV appears that may arise from metal-fluoride compounds such as NiF_2. Note that the Ni surface concentration of the cycled sample is greater than that of the starting sample: the element could be present as a fluorinated compound at the surface of the oxide particles. The P2p spectrum also indicated increased intensities near 135 eV that arise from phosphate species after cycling.

3.4. SIMS on negative electrodes before and after cycling

Fig. 10 presents sputter depth profiles by SIMS for carbon, aluminum, manganese, and nickel which are obtained on graphite-based negative electrodes and which display the changes induced by electrochemical cycling.

The SIMS profile of the pristine as-prepared negative electrode (light blue) serves as the point of reference. The other profiles are collected from negative electrodes harvested from discharged cells containing the cycled as-prepared (black) and the cycled 3.4 nm alumina-coated positive electrodes (red). Note that the count rate in dynamic SIMS is dependent upon the ionization efficiency which heavily depends upon the surface composition and structure during ion irradiation. Therefore, we cannot draw definitive conclusions from differences in count rates for different elements in the same sample. However, the matrix material for all samples is carbon and its counts are the same (~5 × 10^4 cps) within the bulk, allowing us to compare and draw conclusions from cps data for the same element from different samples.

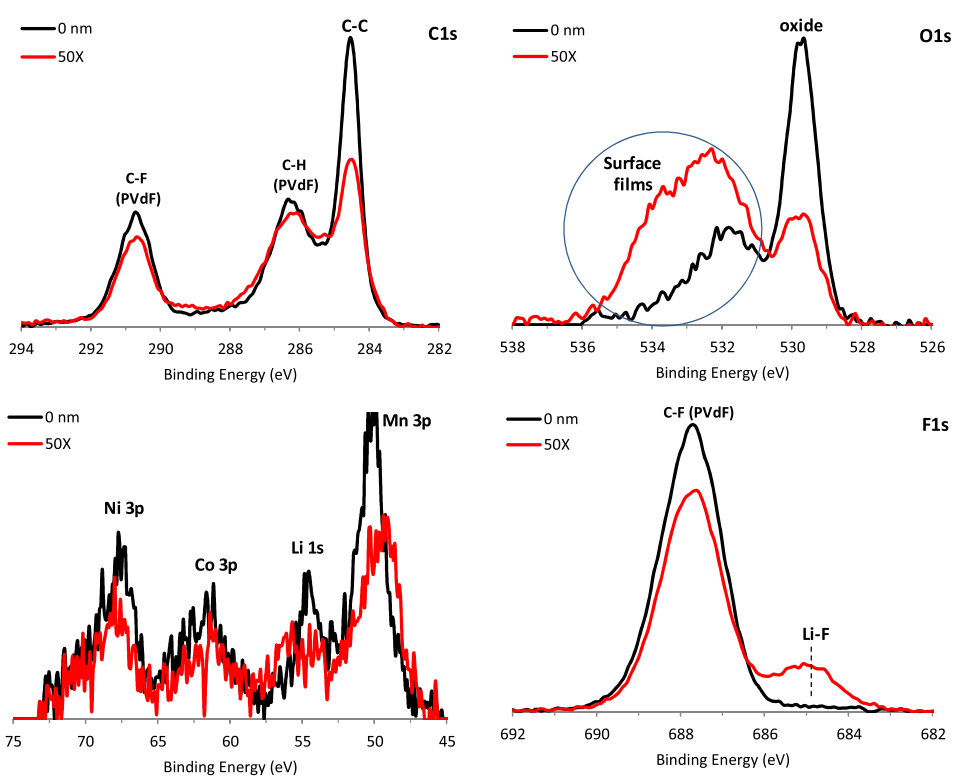

Fig. 8. XPS spectra from the 0 nm (as-prepared) samples before (black lines) and after 50 cycles (red lines) in the 2.2–4.6 V voltage window. (For interpretation of the references to colour in this figure legend, the reader is referred to the web version of this article.)

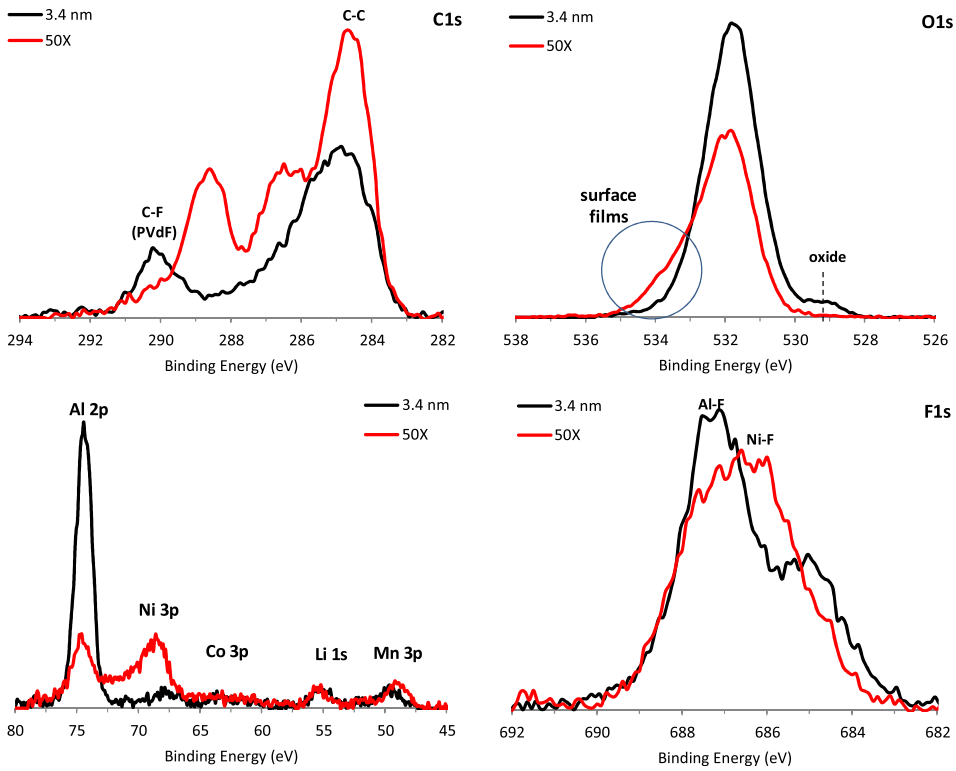

Fig. 9. XPS spectra from the 3.4 nm alumina-coated samples before (black lines) and after 50 cycles (red lines) in the 2.2–4.6 V voltage window. (For interpretation of the references to colour in this figure legend, the reader is referred to the web version of this article.)

The top-left of Fig. 10 shows the carbon signal from the three negative electrodes. The depth profile for the pristine sample is fairly constant as only carbon containing species (such as graphite, SuperP, and binder) constitute the electrode coating. For both cycled samples, the time required for the C-signal to reach levels similar to that of the pristine material is significantly greater: the greatest increase occurs after ~400 s for the negative electrode from the ALD-modified cell vs. ~800 s for the electrode from the cell containing the as-prepared electrodes. The initially higher carbon count rates and shorter sputtering times reveal that the SEI on the negative electrode is thinner for the cycled ALD-modified cell than for the baseline cell.

The Al signals from the three electrodes are plotted in the top-right of Fig. 10. A particularly large amount of Al is present near the surface of the cycled electrode that originates from the ALD-modified cell; the maxima in Al cps coincides with the maximum increase in carbon signal, indicating subsurface enrichment of Al. The Al peak height (~20,000 cps) is significantly larger than that from the pristine electrode (~60 cps), and from the electrode harvested from the baseline cell (~300 cps).

Differences between pristine and cycled materials are also found for manganese, nickel (Fig. 10), and cobalt (not shown here, but cps data qualitatively follow the Ni trends). Their counts are very low in the pristine negative, indicating only trace levels in the electrode. For the cycled sample, the transition metal cps are significantly higher. This feature is most apparent for Mn, which shows a roughly 5 orders of magnitude higher cps at its maximum point; Ni shows a roughly 2 orders of magnitude higher cps. Here also, the maximum in transition-metal cps coincide with the maximum increase in carbon signal. Additional measurements confirm that the total Mn and Ni counts within the negative electrode, obtained by integration, are greater for cells containing the as-prepared than for cells containing the coated positive electrodes.

4. Discussion

Various mechanisms have been proposed to explain improved capacity retention of cells containing an alumina-coated positive electrode. For example, Myung et al. showed that alumina-coated $Li_{1.05}Mn_{0.4}Ni_{0.4}Co_{0.15}O_2$ powders fired at 400 °C display improved capacity retention in cells with both lithium and graphite counter electrodes [21,40]. The improved performance was attributed to transformation of the metal oxide coating layer to metal fluoride during cycling by scavenging F^- from HF in the electrolyte. The effects of this process are two-fold: (i) the metal fluoride layers are more resistant to HF attack; and (ii) lowering the amount of acidic species in the electrolyte reduces the degradation of active material in both electrodes [21,40]. Oh et al. also observed improved capacity retention of alumina-coated $LiCoO_2$ thin films, heat-treated at 400 °C. HF and H_2O scavenging from the electrolyte transformed the alumina coating into an $AlF_3 \cdot 3H_2O$ layer during cycling [20]. Verdier et al. showed the same effect for alumina coatings on $LiCoO_2$, heat-treated at 700 °C. A $LiAl_xCo_{1-x}O_2$ solid solution formed on the $LiCoO_2$ surface inhibiting Co dissolution and its deposition on the graphite negative electrode [41]. Their XPS data on graphite negative electrodes indicated that oxidation products and transition metal ions from the positive are transported through the electrolyte and incorporated into the negative SEI; this observation is in agreement with earlier reports by Abraham et al. [30] and Komaba et al. [42].

All of the above mechanisms, along with others, appear to impact the capacity fade and impedance rise of our full-cells. For instance, capacity fade in our baseline cells results primarily from lithium trapping in the negative electrode SEI; this trapping is enhanced by the presence of transition-metal ions [42]. Our SIMS data show that the negative electrode for an ALD-modified cell contains less Mn, Ni, and Co when compared to that of a baseline

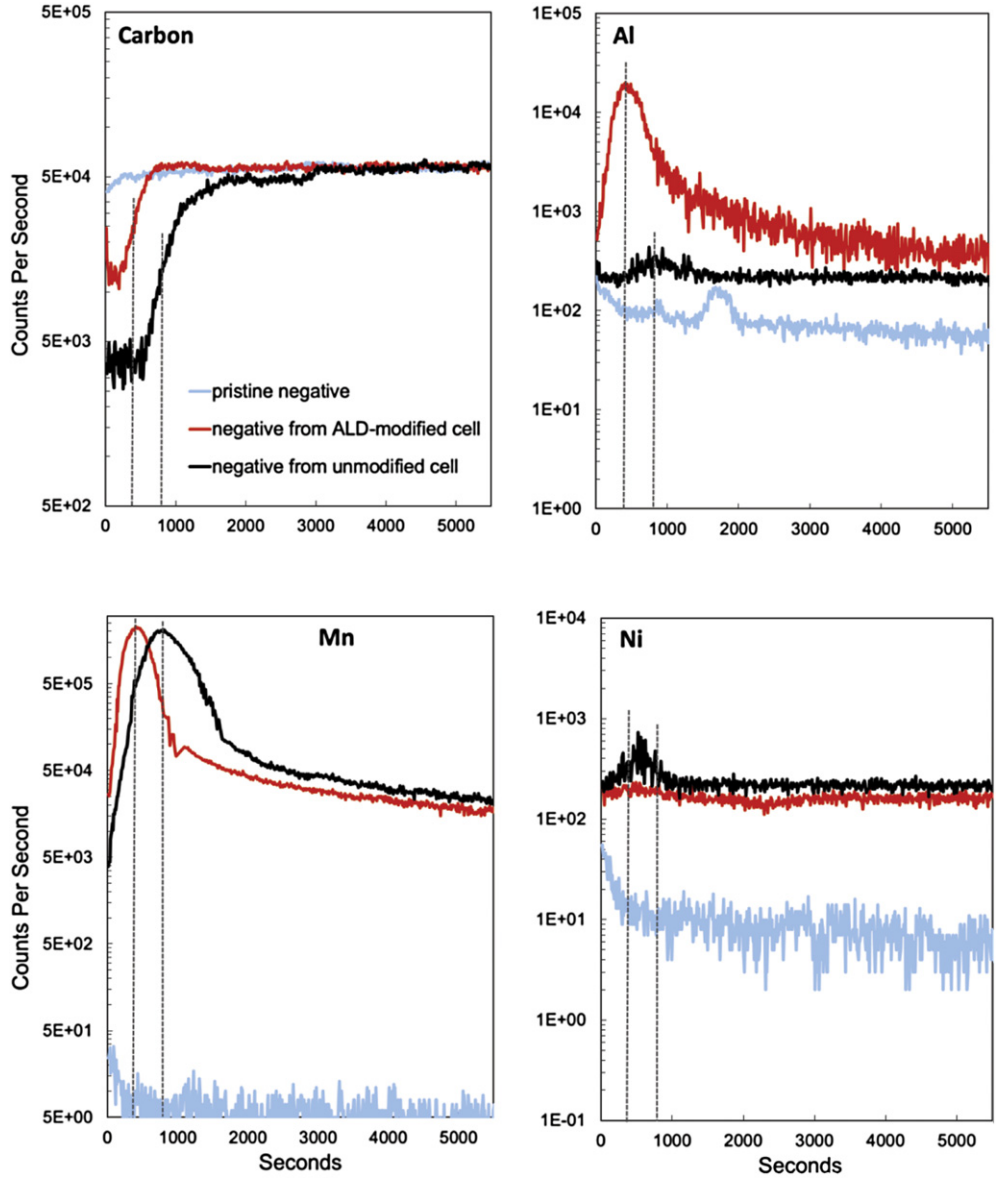

Fig. 10. SIMS sputter depth profiles from negative electrodes for carbon, aluminum, manganese, and nickel. The cells bear the 0 nm (as-prepared) and 3.4 nm alumina-coated positive electrodes, after 50 cycles in the 2.2–4.6 V cycling window at 30 °C. Data from an as-prepared, but pristine, negative electrode is shown for comparison.

cell. That is, the alumina coating on the positive oxide inhibits the dissolution of transition-metal ions that would otherwise be incorporated into the graphite SEI and increase the occurrence of lithium-consuming side reactions. Consequently, the negative electrode SEI is thinner for the ALD-modified cells, as seen in the SIMS data (Fig. 10).

Interestingly, the strong Al SIMS signal indicates that portions of the alumina coating are transported through the electrolyte and incorporated into the negative electrode SEI (a strong Al SIMS signal was also seen on the negative side of the alumina powder-modified cell after 50 cycles). This dissolution explains the reduction of Al2p and O1s (Al–O) XPS peak intensities on cycling. The Al, possibly in the form of AlF_3, $AlPO_4$ or related species, may stabilize the negative SEI and reduce Li trapping. This hypothesis is supported by the improved capacity retention reported for cells containing $AlPO_4$- and alumina-coated graphite negative electrodes [22,43].

We also find much improved capacity retention in our powder-modified cells, in which we add 5 wt. % of nanosized alumina powder to the positive electrode. Our observations agree well with the finding by Lee et al. who reported cycle performance improvements of commercial grade $LiCoO_2$/graphite lithium-ion cells that contained $Al(OH)_3$ powder in the $LiCoO_2$-based positive electrode [44]. These data indicate the importance of effective HF scavenging (via the reaction $Al_2O_3 + 6HF \rightarrow 2AlF_3 + 3H_2O$) for improved capacity retention, explaining in part the good capacity retention for cells in which the alumina coating covers all of the positive electrode constituents. Simultaneous scavenging of H_2O by the coating, important to prevent continuing HF generation, may also play a role, as suggested by Oh et al. [20].

The impedance rise of our cells, during cycling, decreases with increasing thickness of the alumina coating on the positive electrode. In fact, both the high-frequency and mid-frequency impedance arcs are smaller after cycling. The increase in the high-frequency arc results from a degradation of the electron conduction network in the positive electrode. This degradation can be attributed to various factors that include rearrangements in the oxide and carbon constituents; PF_6^- intercalation into the

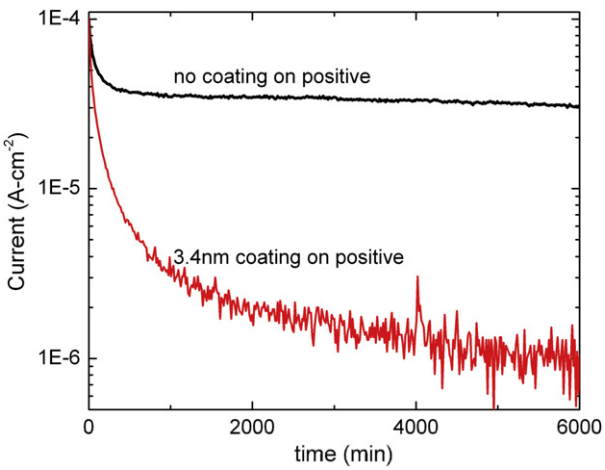

Fig. 11. Current required to maintain 4.7 V vs. Li/Li+ in half-cells containing the baseline and alumina-coated positive electrodes, after 5 initial cycles. The steady-state current for the cell with the alumina-coated positive electrode is about one to two orders of magnitude lower than the cell with the baseline electrode.

carbons; changes in the oxide surface composition induced by elemental dissolution; and a reduction in the electrode's integrity that results from mechanical stresses and strains induced during electrochemical cycling [11,13,45–48]. In our samples, the alumina coating probably reduces the high-voltage intercalation of PF_6^- into the positive electrode graphite. In addition, the smaller high-frequency impedance arcs for the alumina-coated samples may simply be the result of enhancements to the electrode's mechanical integrity; improvements in mechanical integrity from ALD coatings have been reported by other investigators [49,50].

The increase in the mid-frequency impedance arc on cycling arises from features at the oxide–electrolyte interfaces that impede the motion of lithium ions. For example, electrolyte oxidation can produce detrimental reaction products at the electrode–electrolyte interface [51]. In a forthcoming publication, we will also discuss the effects of state-of-charge changes on impedance data. Our XPS data from uncoated positive electrodes show increasing coverage of the electrode constituents by surface films that arise from electrolyte oxidation/decomposition. Fig. 11 shows that the electronically–insulating alumina coating significantly reduces the self-discharge current at 4.7 V of lithium-bearing cells. This current can be regarded as a measure of electrolyte oxidation, assuming that no further reduction occurs on the lithium side. The current for the cell containing the alumina-coated positive electrode is approximately 30 times lower than that for the baseline cell. Similar differences are also observed for cells held at other voltages, 4.5 and 4.6 V for example. Note that reduced self-discharge is crucial to obtain long cycle- and calendar-life.

The alumina coating does not prevent electrolyte oxidation entirely as seen from increased intensities in the C1s and O1s XPS spectra of the cycled samples. The surface films formed on the coated samples are different and apparently more permeable to lithium-ion transport; the energy required for lithium-ion solvation–desolvation processes may also be lower in these altered surface films. These surface films may protect the surfaces of the oxide particles and reduce surface structural transformations that can impede lithium-ion motion. For example, the presence of a $Li_{1-x}Ni_xO$ layer on $LiNi_{0.8}Co_{0.2}O2$ particle surfaces is known to impede lithium motion [11,52,53]. Creation of defect-like spinel structures, on $Li_{1.2}Ni_{0.2}Mn_{0.6}O_2$ particle surface after cycling, has also been reported [54]. These second phases, and phase boundaries introduced by their formation, could create barriers to lithium-ion motion, and hence increase electrode impedance.

A schematic, depicting the mechanisms proposed above, is shown in Fig. 12. The figure highlights the interactions between the positive and negative electrodes. This "cross-talk" can be detrimental to cell performance, as seen from the incorporation of transition metal elements into the graphite SEI. On the other hand, the crossover and incorporation of Al that reduces lithium-consuming reactions on the negative electrode points to its beneficial effects.

The presence of transition metal elements, especially Mn, at the graphite negative electrode is a significant feature of our SIMS data. Previous studies have correlated the accumulation of the transition metal elements in the SEI to impedance rise at the graphite–electrolyte interface [30,45]. However, negative electrode impedance rise is relatively small even in baseline cells. That is, transition metal presence is not the only criterion that governs impedance rise of this electrode; other factors, such as lithium-ion solvation/desolvation kinetics, surface morphology, and electrode

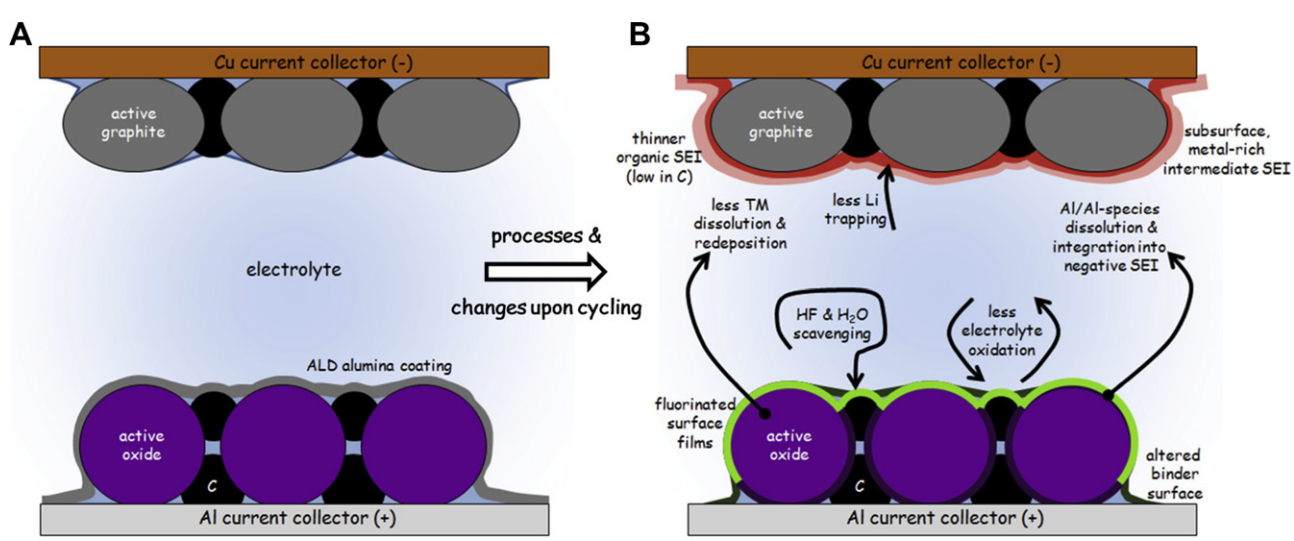

Fig. 12. Schematic highlighting the processes and changes upon cycling of an electrochemical cell that contains an ALD-coated positive LMR-NMC electrode: A) uncycled condition in which an ALD coating covers all constituents of the positive electrode, such as carbon additives, binder, and active oxide particles. B) Upon cycling, the surface films, including the ALD coating, change on both electrodes, positive and negative, due to electrochemical cross-talk, and differ distinctly from unmodified cells.

composition/design may play a bigger role in determining charge transfer at the graphite–electrolyte interface.

Our data show that cell performance improves with increasing thickness of the alumina coating. In addition to scavenging detrimental species from the electrolyte, a thicker coating reduces electrolyte oxidation, metal-ion dissolution, and may even provide enhanced mechanical stability. Beyond a certain thickness, however, Li-ion transport across the alumina coating is expected to slow down. In fact, additional experiments show that cell impedances begin to increase for >4 nm thick alumina coatings on the positive electrode. We have also examined the effect of alumina ALD coatings applied to the negative electrode: our findings indicate that only very thin alumina coatings (up to 0.5 nm) improve full cell performance; thicker coatings worsen capacity retention. Thus, coating (and modifying) the positive electrodes appears to be the most effective means to improve full-cell performance.

5. Conclusions

Cells containing ALD alumina-coated and alumina-powder modified $Li_{1.2}Ni_{0.15}Mn_{0.55}Co_{0.1}O_2$-based positive electrodes and graphite-based negative electrodes show improved performance when electrochemically cycled at 30 °C in the 2.2–4.6 V voltage range. The lowest impedance rise and highest capacity retention is achieved for a 3.4 nm thick ALD alumina coating, outperforming our full-cells that contain ALD coatings applied to the negative electrode and alumina-powder modified positive electrodes. Other conclusions from our data include the following:

1. All constituents of the composite electrode are coated by alumina during the ALD process. Peak shifts in the XPS spectra suggest Al-doping of the PVdF binder.
2. The ALD thicknesses at the top-surface of the rough composite electrodes are estimated by a new approach using XPS signal intensity measurements.
3. Capacity retention improves with increasing thickness (up to 3.4 nm) of the alumina coating on the positive electrode; improved capacity retention is also observed for the alumina-powder modified cells. The alumina converts to AlF_3 and captures detrimental species, such as HF, from the electrolyte that would otherwise etch/degrade the electrode active materials and dissolve transition metal ions.
4. Capacity fade in our baseline full-cells is primarily governed by trapping of lithium on the negative side, and not by cell impedance rise. The alumina coating helps to reduce dissolution of Mn, Ni, and Co from the positive electrode which helps to stabilize the negative SEI. Incorporation of Al-species may further help to stabilize the SEI. Lithium consumption on the negative side is thereby reduced.
5. In the absence of a coating on the positive electrode, cell impedance rise during cycling occurs primarily from slower charge-transfer processes on the positive electrode. Impedance rise is related to failure of the electron-conducting network (high-frequency arc) and slower ionic transport across the electrolyte–oxide interfaces (mid-frequency arc).
6. When a coating is applied, the cell impedance after cycling decreases with increasing thickness of the alumina coating. It is not reduced in alumina-powder modified cells. The coatings may lessen the high-frequency arc increase by reducing PF_6^- intercalation into the positive electrode carbons, and by enhancing mechanical integrity of the electrode. The smaller ionic impedances may be the result of altered surface films and reduced structural transformations at the oxide–electrolyte interface.
7. The coatings reduce electrolyte decomposition.
8. The alumina coatings inhibit, but do not entirely prevent, the dissolution of Mn, Ni, and Co.
9. The ALD alumina coatings are found to be chemically unstable. Because of this, the alumina-modifications, ALD-coating and powder-blending, delay, but do not prevent, full-cell performance degradation during extended cycling/aging.

Acknowledgments

Support from the U.S. Department of Energy's Vehicle Technologies Program, specifically from Peter Faguy and Dave Howell, is gratefully acknowledged. We also acknowledge valuable discussions with D. Dees, J. Bareno, and Y. Zhu (at Argonne). The submitted manuscript has been created by UChicago Argonne, LLC, Operator of Argonne National Laboratory ("Argonne"). Argonne, a U.S. Department of Energy Office of Science laboratory, is operated under Contract No. DE-AC02-06CH11357. The U.S. Government retains for itself, and others acting on its behalf, a paid-up nonexclusive, irrevocable worldwide license in said article to reproduce, prepare derivative works, distribute copies to the public, and perform publicly and display publicly, by or on behalf of the Government. We are grateful to B. Polzin, A. Jansen, and S. Trask from the U.S. Department of Energy's (DOE) Cell Fabrication Facility (CFF), Argonne. The CFF is fully supported by the DOE Vehicle Technologies Program (VTP) within the core funding of the Applied Battery Research (ABR) for Transportation Program. Use of the Center for Nanoscale Materials was supported by the U. S. Department of Energy, Office of Science, Office of Basic Energy Sciences, under Contract No. DE-AC02-06CH11357. The work was carried out in part in the Frederick Seitz Materials Research Laboratory Central Facilities, University of Illinois at Urbana-Champaign (UIUC). We're grateful to E. Sammann (at UIUC) for his many significant suggestions and comments.

References

[1] M.M. Thackeray, C. Wolverton, E.D. Isaacs, Energy Environ. Sci. 5 (2012) 7854.
[2] J.-M. Tarascon, Phil. Trans. R. Soc. A 368 (2010) 3227.
[3] B. Kang, G. Ceder, Nature 458 (2009) 190.
[4] S.-H. Kang, P. Kempgens, S. Greenbaum, A.J. Kropf, K. Amine, M.M. Thackeray, J. Mater. Chem. 17 (2007) 2069.
[5] M.M. Thackeray, S.-H. Kang, C.S. Johnson, J.T. Vaughey, R. Benedek, S.A. Hackney, J. Mater. Chem. 17 (2007) 3112.
[6] Z. Lu, D.D. MacNeil, J.R. Dahn, Electrochem. Solid State Lett. 4 (2001) A191.
[7] D. Aurbach, J. Power Sources 89 (2000) 206.
[8] A.M. Andersson, D.P. Abraham, R. Haasch, S. MacLaren, J. Liu, K. Amine, J. Electrochem. Soc. 149 (2002) A1358.
[9] D.P. Abraham, J. Liu, C.H. Chen, Y.E. Hyung, M. Stoll, N. Elsen, S. MacLaren, R. Twesten, R. Haasch, E. Sammann, I. Petrov, K. Amine, G. Henriksen, J. Power Sources 119–121 (2003) 511.
[10] D.P. Abraham, J.L. Knuth, D.W. Dees, I. Bloom, J.P. Christophersen, J. Power Sources 170 (2007) 465.
[11] D. Dees, E. Gunen, D. Abraham, A. Jansen, J. Prakash, J. Electrochem. Soc. 152 (2005) A1409.
[12] M. Kerlau, M. Marcinek, V. Srinivasan, R.M. Kostecki, Electrochim. Acta 52 (2007) 5422.
[13] R. Kostecki, F. McLarnon, Electrochem. Solid State Lett. 7 (2004) A380.
[14] B. Xu, C.R. Fell, M. Chi, Y.S. Meng, Energy Environ. Sci. 4 (2011) 2223.
[15] Y. Zhu, Y. Li, M. Bettge, D.P. Abraham, J. Electrochem. Soc. 159 (2012) A2109.
[16] Z. Chen, Y. Qin, K. Amine, Y.-K. Sun, J. Mater. Chem. 20 (2010) 7606.
[17] Y.S. Jung, A.S. Cavanagh, A.C. Dillon, M.D. Groner, S.M. George, S.-H. Lee, J. Electrochem. Soc. 157 (2010) A75.
[18] K.T. Lee, S. Jeong, J. Cho, Accounts of Chemical Research 2012, http://dx.doi.org/10.1021/ar200224h.
[19] M.M. Thackeray, C.S. Johnson, J. Kim, K.C. Lauzze, J.T. Vaughey, N. Dietz, D. Abraham, S.A. Hackney, W. Zeltner, M.A. Anderson, Electrochem. Commun. 5 (2003) 752.
[20] Y. Oh, D. Ahn, S. Nam, B. Park, J. Solid State Electrochem. 14 (2010) 1235.
[21] S.-T. Myung, K. Izumi, S. Komaba, Y.-K. Sun, H. Yashiro, N. Kumagai, Chem. Mater. 17 (2005) 3695.
[22] Y.S. Jung, A.S. Cavanagh, L.A. Riley, S.-H. Kang, A.C. Dillon, M.D. Groner, S.M. George, S.-H. Lee, Adv. Mater. 22 (2010) 2172.

[23] Y.S. Jung, A.S. Cavanagh, Y. Yan, S.M. George, A. Manthiram, J. Electrochem. Soc. 158 (2011) A1298.
[24] I.D. Scott, Y.S. Jung, A.S. Cavanagh, Y. Yan, A.C. Dillon, S.M. George, S.-H. Lee, Nano Lett. 11 (2011) 414.
[25] J.-T. Lee, F.-M. Wang, C.-S. Cheng, C.-C. Li, C.-H. Lin, Electrochim. Acta 55 (2010) 4002.
[26] S.M. George, Chem. Rev. 110 (2010) 111.
[27] J.C. Wang, M. Gaffari, S. Choi, J. Chem. Phys. 63 (1975) 772.
[28] R.L. Puurunen, J. Appl. Phys. 97 (2005) 121301.
[29] K.G. Gallagher, S.-H. Kang, S.U. Park, S.Y. Han, J. Power Sources 196 (2011) 9702.
[30] D.P. Abraham, T. Spila, M.M. Furczon, E. Sammann, Electrochem. Solid State Lett. 11 (2008) A226.
[31] Y. Cho, J. Cho, J. Electrochem. Soc. 157 (2010) A625.
[32] M.-S. Park, J.-W. Lee, W. Choi, D. Im, S.-G. Doo, K.-S. Park, J. Mater. Chem. 20 (2010) 7208.
[33] A.R. Armstrong, M. Holzapfel, P. Novak, C.S. Johnson, S.-H. Kang, M.M. Thackeray, P.G. Bruce, J. Am. Chem. Soc. 128 (2006) 8694.
[34] E. Barsoukov, in: E. Barsoukov, J.R. MacDonald (Eds.), Impedance Spectroscopy – Theory, Experiment, and Applications, second ed., John Wiley, 2005 (Chapter 4.5).
[35] D.P. Abraham, DOE Vehicle Technologies Program, Annual Merit Review (AMR), May 14–18, 2012, http://www1.eere.energy.gov/vehiclesandfuels/pdfs/merit_review_2012/.
[36] L.B. Biedermann, M.L. Bolen, M.A. Capano, D. Zemlyanov, R.G. Reifenberger, Phys. Rev. B 79 (2009) 125411.
[37] S. Tanuma, C.J. Powell, D.R. Penn, Surf. Interface Anal. 36 (2004) 1.
[38] B. Xu, C.N. Borca, S. Ducharme, A.V. Sorokin, P.A. Dowben, V.M. Fridkin, S.P. Palto, N.N. Petukhova, S.G. Yudin, J. Chem. Phys. 114 (2001) 1866.
[39] D.S. Kim, Y.Y. Yu, K. Char, J. Appl. Phys. 96 (2004) 2278.
[40] S.-T. Myung, K. Izumi, S. Komaba, H. Yashiro, H.J. Bang, Y.-K. Sun, N. Kumagai, J. Phys. Chem. C 111 (2007) 4061.
[41] S. Verdier, L. Ouatani, R. Dedryvère, F. Bonhomme, P. Biensan, D. Gonbeau, J. Electrochem. Soc. 154 (2007) A1088.
[42] S. Komaba, N. Kumagai, Y. Kataoka, Electrochim. Acta 47 (2002) 1229.
[43] S.-E. Lee, E. Kim, J. Cho, Electrochem. Solid State Lett. 10 (2007) A1.
[44] H. Lee, H.-J. Kim, D. Kim, S. Choi, J. Power Sources 176 (2008) 359.
[45] D.H. Jang, S.M. Oh, J. Electrochem. Soc. 144 (1997) 3342.
[46] T. Ishihara, M. Koga, H. Matsumoto, M. Yoshio, Electrochem. Solid State Lett. 10 (2007) A74.
[47] J.A. Seel, J.R. Dahn, J. Electrochem. Soc. 147 (2000) 892.
[48] V.A. Sethuraman, N.V. Winkle, D.P. Abraham, A.F. Bower, P.R. Guduru, J. Power Sources 206 (2012) 334.
[49] L.A. Riley, A.S. Cavanagh, S.M. George, S.-H. Lee, A.C. Dillon, Electrochem. Solid State Lett. 14 (2011) A29.
[50] H. Wu, G. Chan, J.W. Choi, Ill Ryu, Y. Yao, M.T. McDowell, S.W. Lee, A. Jackson, Y. Yang, L. Hu, Y. Cui, Nat. Nanotechnol. 7 (2012) 310.
[51] M. Moshkovich, M. Cojocaru, H.E. Gottlieb, D. Aurbach, J. Electroanal. Chem. 497 (2001) 84.
[52] D.P. Abraham, R.D. Twesten, M. Balasubramanian, J. Kropf, D. Fischer, J. McBreen, I. Petrov, K. Amine, J. Electrochem. Soc. 150 (2003) A1450.
[53] S. Zheng, R. Huang, Y. Makimura, Y. Ukyo, C.A.J. Fisher, T. Hirayama, Y. Ikuhara, J. Electrochem. Soc. 158 (2011) A357.
[54] C.R. Fell, M. Chi, Y.S. Meng, J.L. Jones, Sol. State Ionics 207 (2012) 44.